An Idealised Model Study of Eddy Energetics in the Western Boundary 'Graveyard'

ZHIBIN YANG

Key Laboratory of Physical Oceanography, Ocean University of China, Qingdao, China, and College of Oceanography, Hohai University, Nanjing, China, and Centre for Ocean and Atmospheric Sciences, School of Environmental Sciences, University of East Anglia, Norwich, United Kingdom, and Department of Atmospheric and Oceanic Sciences & Institute of Atmospheric Sciences, Fudan University, Shanghai, China

XIAOMING ZHAI

Centre for Ocean and Atmospheric Sciences, School of Environmental Sciences, University of East Anglia, Norwich, United Kingdom

DAVID P. MARSHALL

Department of Physics, University of Oxford, Oxford, United Kingdom

GUIHUA WANG

Department of Atmospheric and Oceanic Sciences & Institute of Atmospheric Sciences, Fudan University, Shanghai, China, and CMA-FDU Joint Laboratory of Marine Meteorology, Fudan Univerisity, Shanghai, China

Corresponding author: Xiaoming Zhai, xiaoming.zhai@uea.ac.uk

Abstract:

Recent studies show that the western boundary acts as a 'graveyard' for westward-propagating ocean eddies. However, how the eddy energy incident on the western boundary is dissipated remains unclear. Here we investigate the energetics of eddy-western boundary interaction using an idealised MIT ocean circulation model with a spatially variable grid resolution. Four types of model experiments are conducted: (1) single eddy cases, (2) a sea of random eddies, (3) with a smooth topography and (4) with a rough topography. We find significant dissipation of incident eddy energy at the western boundary, regardless of whether the model topography at the western boundary is smooth or rough. However, in the presence of rough topography, not only the eddy energy dissipation rate is enhanced, but more importantly, the leading process for removing eddy energy in the model switches from bottom frictional drag as in the case of smooth topography to viscous dissipation in the ocean interior above the rough topography. Further analysis shows that the enhanced eddy energy dissipation in the experiment with rough topography is associated with greater anticyclonic-ageostrophic instability (AAI), possibly as a result of lee wave generation and non-propagating form drag effect.

1. Introduction

There is increasing evidence in support of the idea that the available potential energy built up by large-scale wind Ekman pumping of the main thermocline is released by the generation of eddies through instabilities of the mean currents (e.g., Gill et al. 1974; Wunsch 1998; Zhai and Marshall 2013). In equilibrium, the energy flux into the eddy field has to be balanced by dissipation. However, where and how eddy energy is dissipated remains poorly understood (Ferrari and Wunsch 2009). Zhai et al. (2010) used a simple reduced-gravity model along with satellite altimetry data to show that the western boundary acts as a 'graveyard' for westward-propagating ocean eddies, raising the possibility that the western boundary may be a hot spot for ocean mixing. They estimated a convergence of eddy energy near the western boundary of approximately 0.1-0.3 TW (1 TW = 10^{12} W) poleward of 10 degree in latitude, a significant fraction of the wind power input to the ocean general circulation (e.g., Wunsch 1998; Hughes and Wilson 2008; Zhai et al. 2012). They further argued following Dewar and Hogg (2010) that this energy is most likely scattered into high-wavenumber vertical modes, resulting in energy dissipation and diapycnal mixing. However, the depth-integrated eddy energy budget approach and the use of a reduced-gravity model in Zhai et al. (2010) enabled them to show regions of energy loss for ocean eddies, but failed to identify the physical processes that are responsible for the eddy energy loss.

The potential candidate processes for dissipating eddy energy include direct damping by air-sea interactions (Duhaut and Straub 2006; Zhai and Greatbatch 2007; Hughes and Wilson 2008; Xu et al. 2016), bottom frictional drag (Sen et al. 2008; Arbic et al. 2009), loss of balance (Molemaker et al. 2005; Williams et al. 2008; Alford et al. 2013), and energy transfer to lee waves over rough bottom topography (Nikurashin and Ferrari 2010a; Nikurashin et al. 2013). Importantly, some of the dissipating processes such as the bottom friction remove eddy energy adiabatically, while other processes such as lee wave generation over rough topography may lead to bottom-enhanced diapycnal mixing in the western boundary region. There are fragments of evidence suggesting elevated bottom-enhanced energy dissipation and diapycnal mixing at the western boundary of the North Atlantic (Walter et al. 2005; Stöber et al. 2008; Clément et al. 2016), but these observations are highly limited in space and time, rendering them hard to interpret. Therefore, the fate of the eddy energy that converges on the western boundary remains elusive.

Here we conduct a high-resolution idealized model study of eddy energetics in the western boundary region, with a particular focus on the effect of rough bottom topography. The paper is organized as follows. We begin in Section 2 by describing the model setup and experiment design. In Section 3, we present and compare results from model experiments with different initial conditions and bottom topography and discuss the role of different instability processes. In Section 4, we apply a Lagrangian filer to diagnose lee wave energy dissipation and discuss the roles of non-propagating form drag and arrested topographic waves. Finally, the paper concludes with a summary in Section 5.

2. Model Experiments

a. Model configuration

We employ the non-hydrostatic configuration of the Massachusetts Institute of Technology general circulation model (MITgcm; Marshall et al. 1997). The model domain is a rectangular basin that is 491 km (717 km for the random eddies case) wide in the zonal direction, 985 km long in the meridional direction and 3 km deep, with a continental slope situated next to the western boundary. Sponge layers are applied at the northernmost, southernmost and easternmost of the model domain to damp out any waves approaching these boundaries. The model simulations are initialized with either a single eddy or a sea of random eddies in the deep ocean to the east of the continental slope

(Table 1). In order to effectively simulate eddy-topography interaction, we use a uniform 20 m resolution in the vertical but a spatially variable horizontal resolution ranging from about 5 km in the deep ocean to 400 m in the slope region (Fig. 1). The MITgcm with a variable horizontal grid resolution was also used by Dewar and Hogg (2010) to achieve fine resolution near a western wall in order to better simulate eddy induced temperature overturns and mixing. The model is set on a beta-plane with $f_0 = 5\times10^{-5}$ s^{-1} and $\beta = 2.15\times10^{-11}$ m^{-1} s^{-1} and employs a linear equation of state with no salinity such that the model density depends only on temperature. We employ the K-profile parameterisation (KPP) vertical mixing scheme (Large et al. 1994) and a quadratic bottom friction with drag coefficient of $C_d = 2\times10^{-3}$. Following Nikurashin et al. (2013), we set the Laplacian horizontal and vertical viscosity values to $A_h = 1$ m^2 s^{-1} and $A_v = 10^{-3}$ m^2 s^{-1} respectively, and both horizontal and vertical diffusivities for temperature to 10^{-5} m^2 s^{-1}. A large ratio of viscosity to diffusivity is used here to ensure that energy at small scales is dissipated primarily by viscous processes and the effect of both explicit and spurious diffusion on the flow energetics is small.

b. Topography

In the control experiment, a smooth hyperbolic tangent function, uniform in the meridional direction, is used for the shape of the continental slope near the western boundary (Fig. 2a). Similar to Wang and Stewart (2018), the bathymetry $h(x)$ is defined by:

$$h(x) = -Z_s - \frac{1}{2} H_s \tanh\left(\frac{x - X_s}{W_s}\right), \quad (1)$$

where x is the offshore distance (km), $Z_s = 1600$ m is the vertical slope position, $H_s = 2800$ m is the shelf height, $X_s = 120$ km is the offshore slope position, and $W_s = 50$ km is the slope half-width. The values in (1) are chosen such that the smooth topography resembles the average shape of the observed continental slope at the western boundary in the North Pacific (between 10°N and 45°N) which is typical of continental slopes at other western boundaries.

In the rough-topography experiment, synthetically-generated rough topography that includes horizontal scales in the range from 1 to 40 km is added onto the smooth topography in the high resolution (400 m) region on the continental slope (Fig. 2b). The synthetic topography is computed as a sum of Fourier modes with amplitudes given by the observed topographic spectrum near the western boundary and random phases, following the stochastic seafloor model proposed by Goff and Jordan (1988). The Goff and Jordan model is a topographic spectrum model at O(0.1-100) km scales based on a statistical description of abyssal hills,

$$P(k,l)_{GJ} = \frac{2\pi h^2(\mu-2)}{k_0 l_0}\left[1+\frac{k^2}{k_0^2}\cos^2(\phi-\phi_0)+\frac{l^2}{l_0^2}\sin^2(\phi-\phi_0)\right]^{-\mu/2}, \quad (2)$$

where (k, l) are the horizontal wavenumbers in the zonal and meridional directions, ϕ is the angle between the wave vector and the eastward direction, h^2 is the variance of the topographic height, (k_0, l_0) are the characteristic wavenumbers of the principal axes of anisotropy, ϕ_0 is the azimuthal angle, and μ is the high-wavenumber roll-off slope.

Here we use the high-resolution multibeam topography data from the U.S. National Geophysical Data Center (NGDC, https://www.ncei.noaa.gov/maps-and-geospatial-products) to estimate the spectral characteristics of small-scale topography near the western boundary. The multibeam topography data located in the Kuroshio region (19-23°N, 123-127°E) is first divided in 9 segments of size 0.5°×0.5°. In each segment, the large-scale topographic slope is removed by fitting a slope plane before computing the topographic spectrum. Finally, the mean parameters of those 9 segments are used to construct the rough topography. Given the idealized nature of our model study, we follow Nikurashin and Ferrari (2010b) and assume for simplicity that the synthetic rough topography is isotropic in our model. Two synthetic rough topographies (rough 1 and rough 2) are generated with the same spectral amplitude but different random phases for use in model experiments initialized with a single anticyclonic eddy.

c. Initial conditions

An eddy structure model in cyclogeostropic balance is used to construct the initial eddy field in the single eddy experiment (Lee and Niiler 1998),

$$V_\theta = V_0 \times \frac{r}{a} \exp\left[\frac{1}{2}\left(1-\frac{r^2}{a^2}\right)\right] \exp(\lambda z), \quad (3)$$

$$T_\mathrm{i} = T(z) + \frac{V_0 \lambda f a \cdot \exp(\lambda z)}{ag}\left\{\exp\left[\frac{1}{2}\left(1-\frac{r^2}{a^2}\right)\right] + \frac{V_0 \exp(\lambda z)}{fa} \exp\left(1-\frac{r^2}{a^2}\right)\right\}, \quad (4)$$

where a = 33 km (one third of the eddy radius), V_θ is the tangential velocity, V_0 = 0.5 m s^{-1} is the maximum velocity, g is the acceleration of gravity (9.81 m s^{-2}), f is Coriolis frequency, $\lambda = 10^{-3}$ m^{-1}. $T(z)$ is the background temperature derived from Global Digital Environmental Model (GDEM, https://www.usgodae.org//pub/outgoing/static/ocn/gdem) climatological monthly mean temperature (Teague et al. 1990). Since the anticyclonic eddy (AE) and cyclonic eddy (CE) tend to drift slightly equatorward and poleward respectively as they propagate westward, we initialize the AE (CE) in the northeast (southeast) of the domain to make sure the eddy encounters the continental slope in the high-resolution region (Figs. 3a-b). Other configurations for AE and CE are the same.

Following Zhai et al. (2010) and towards a more realistic simulation, we also conduct experiments initialized with a sea of random eddies. In these experiments (Random hereafter), the initial sea surface height (SSH) field is constructed to have a magnitude comparable with that in the single eddy case, via superposition of zonal and meridional Fourier modes (Brannigan et al. 2015). For the initial three-dimensional temperature field associated with the eddies, we make use of the vertical eddy temperature anomaly profile derived from the Argo-composite data in the Kuroshio region (Zhang et al. 2013). The background temperature stratification in Random is the same as that in the single eddy cases. The initial eddy velocity field is then derived from a combination of SSH and temperature anomalies via geostrophic balance. The Random experiment is first run at a coarser resolution of 4×4 km for 5 days to allow for the initial adjustment before it is run on the finer spatially-variable grid for 300 days with either a smooth or rough topography (Fig. 3c).

3. Results

3.1. Single eddy experiments

a. Eddy trajectory and amplitude

Fig. 4 shows the trajectories and amplitudes of eddy cores (defined here as positions of maximum/minimum SSH for AE/CE) in the five experiments that are initialized with a single eddy. The eddy trajectories in the smooth- and rough-topography experiments are very similar in the first ~80 days before they approach the slope regions that are shallower than ~1500 m (Fig. 4a). The eddy propagates westward at speeds close to the phase speeds of long Rossby waves, with the AE drifting slightly equatorward and the CE drifting slightly poleward, similar to what has been observed in satellite altimeter data (Chelton et al. 2007). Upon encountering the slope region, the eddies in the control experiments appear to move offshore temporarily, while the eddies in the rough-topography experiments continue to propagate westward and eventually leave the high-resolution region where the synthetically-generated rough topography is added (black box in Fig. 4a). The eddy amplitudes show a general decay with time in all five experiments, with the decay rate being greater in the rough-topography experiments (Fig. 4b).

b. Energetics

We derive the energy equations (see Appendix) and then calculate individual term in the total energy equation following the model algorithm by making use of the MITgcm package for diagnosing the momentum balance. The high-resolution region near the western boundary enclosed by the gray box in Fig. 1 is where the eddy energy budget analysis is conducted. Fig. 5 shows the time series of cumulative energy flux into the box (black solid), cumulative energy dissipation within the box (blue), cumulative diffusive energy flux across the boundaries of the box (green), total energy within the box (red) and the residue (black dashed) for the five single eddy experiments. The energy budget is closed for all five experiments. From the cumulative energy flux, we can infer that the eddies completely enter the high-resolution box region at about day 70. After that, little energy leaves the box, especially for the control experiments. The diffusive energy flux into and out of the box is very small such that the change of total energy within the box is caused by energy flux into the box and dissipation of energy within the box by bottom drag and viscous friction in all five experiments. On the other hand, energy dissipation rates in the rough-topography experiments are considerably higher than those in the control experiments. For example, the accumulated energy dissipation by day 200 in the rough-topography experiment is 1.7×10^{14} J (1.9×10^{14} J) for single CE (AE) comparing to 1.4×10^{14} J (1.7×10^{14} J) in the control experiment, representing an increase of about 21% (12%).

We now compare the relative importance of different energy dissipation terms in the control and rough-topography experiments in the high-resolution region on the continental slope (Fig. 6). As the eddy approaches the western boundary, the magnitudes of both bottom frictional dissipation and interior viscous dissipation increase, regardless of whether the model has a smooth or rough topography, until they reach peak values at approximately day 100 when the eddy comes into close contact with the continental slope. After that, the energy dissipation rates start to decrease in all five experiments due to either the eddies moving slightly offshore in the control experiments or eddies drifting out of the computational region in the rough-topography experiments (Fig. 4a). Consistent with the study of Nikurashin et al. (2013), we find that energy dissipation by the bottom drag is much more important for the smooth-topography control experiments, accounting for nearly half of the total energy dissipation between day 81 and day 120. When the rough topography is present, both the horizontal and vertical viscous energy dissipations in the ocean interior above the topography are greatly enhanced. The maximum horizontal and vertical viscous dissipations in the rough-topography experiments are almost three times and twice, respectively, of those in the control experiments. As a result, energy dissipation by the bottom drag makes the smallest contribution to the total energy dissipation in the rough-topography experiments. Results from the single eddy experiments therefore show that the presence of rough topography on the western boundary continental slope significantly enhances energy dissipation of westward-propagating eddies in the ocean interior, which potentially leads to enhanced mixing and water mass transformation. Comparison of results from the single AE experiments with two different randomly-generated rough topographies (rough 1 and rough 2) further shows that this conclusion is not sensitive to the details of the rough topography used (Figs. 5 and 6).

Since the difference in energy dissipation between the control and rough-topography experiments mainly occurs between day 81 and day 120 (Fig. 6), we now take a closer look at the spatial distribution of energy dissipation in these 40 days. Fig. 7 shows the along slope mean dissipation rates in the high-resolution region integrated over these 40 days. In the two control experiments where the topography is smooth, high dissipation rates are found only in the upper 1000 m due to the large velocity shear associated with the surface-intensified eddy velocity structure (Figs. 7a, d). In contrast, in the rough-topography experiments, in addition to the high energy dissipation rates in the upper water column, there is also a band of marked high energy dissipation that is a few hundred meters wide along and above the rough topography (Figs. 7b, e, g). The difference in energy dissipation rate near the bottom between the control and rough-topography experiments can be as large as a factor of ten (Figs. 7c, f, h), which, to a large extent, explains the energy dissipation differences seen in Fig. 6. Quantitatively, the time- and volume-integrated energy dissipation rate over the high-resolution region on the continental slope between day 81 and day 120 is 2.3×10^{13} J (2.8×10^{13} J) in the CE (AE) control experiment and 4.7×10^{13} J (5.4×10^{13} J, 5.0×10^{13} J) in the CE (AE rough1, AE rough 2) rough-topography experiment, representing an increase of about 104% (93%, 79%).

c. Ageostrophic kinetic energy

The bottom-enhanced dissipation in the rough-topography experiments suggests a significant increase in small-scale ageostrophic motions near the bottom after the eddies encounter the rough topography on the continental slope. Fig. 8 shows the along slope mean ageostrophic kinetic energy integrated between day 81 and day 120 in the five single eddy experiments. The ageostrophic kinetic energy is calculated from the ageostrophic velocity which is taken here as the difference between the total velocity and its geostrophic component. Large ageostrophic kinetic energy is found in the upper 1000 m in all five experiments. In the rough-topography experiments, however, there is also a band of large ageostrophic kinetic energy above the rough topography along the slope, which mirrors the distribution of the high energy dissipation rates. The magnitude of near-bottom ageostrophic kinetic energy in the rough-topography experiments can be ten times larger than that in the control experiments. The differences in ageostrophic energy in the upper 1000 m are largely due to different eddy trajectories in the control and rough-topography experiments (Fig. 4a).

d. Loss of balance

The close connection between small-scale dissipation and ageostrophic motions suggests that loss of balance (LOB) may be responsible for this forward energy cascade. After examining the breakdown of balanced evolution in stratified flow, McWilliams and Yavneh (1998), McWilliams

(2003), and Molemaker et al. (2005) proposed the following LOB instability criteria and instability processes:

(i) sign change of stratification N^2 (gravitational instability or GI);

(ii) Ertel potential vorticity (PV) takes the opposite sign of the planetary vorticity. In the Northern Hemisphere, that means negative PV, i.e.,

$$PV = \underbrace{\left(\nabla \times \mathrm{u}\right)_H \cdot \nabla_H b}_{PV_H} + \underbrace{\left(f + \xi\right)\frac{\partial b}{\partial z}}_{PV_Z} < 0.$$

If it is the first term, i.e., the horizontal component PV_H, that is responsible for the negative PV, the instability that arises is symmetric instability or SI. If it is the second term, i.e., the vertical component PV_Z, that is responsible for the negative PV, the instability that arises is inertial instability or INI;

(iii) sign change of $A - |S| < 0$, where A is the absolute vorticity and

$S = \sqrt{\left(\frac{\partial u}{\partial x} - \frac{\partial v}{\partial y}\right)^2 + \left(\frac{\partial v}{\partial x} + \frac{\partial u}{\partial y}\right)^2}$ is the horizontal strain rate in isopycnal coordinates (anticyclonic-ageostrophic instability or AAI). Note that the criteria of $A - |S| < 0$ is not the sharp boundary for AAI, but rather an indicator of the neighbourhood for its occurrence;

(iv) the Richardson number Ri < 0.25 (Kelvin-Helmholtz instability or KHI).

In (ii)-(iv), stable stratification is assumed, i.e., $N^2 > 0$. Table 2 shows the mean probabilities of occurrence (in percentage) of LOB during day 81-120. Except for the AAI in the rough-topography experiments (bold), conditions for other LOB are rarely satisfied. We note that the probability of occurrence of GI and KHI may be underestimated in our model, since when the criteria in (i) and (iv) are met at scales close to the grid scale, they will be instantaneously re-set to marginally stable conditions by KPP. Fig. 9 shows the along slope mean probabilities of occurrence of AAI during these 40 days. In the control experiments, the probabilities of AAI are only scattered at the shallow end of the slope and also an order of magnitude smaller than those in the rough-topography experiments. In the rough-topography experiments, in additional to high probabilities of AAI at the shallow end of the slope, AAI also consistently exhibits strong near-bottom enhancement in a pattern very similar to those of energy dissipation rates (Fig. 7) and ageostrophic kinetic energy (Fig. 8). Even though the domain-averaged probabilities of AAI in the rough-topography experiments are less than 0.3% (Table 2), local probabilities of AAI near the bottom can be as large as 10%. Furthermore, there is also a close temporal correspondence between the probabilities of occurrence of AAI and interior viscous energy dissipation rates in all three rough-topography experiments, whereas in the control experiments where the probabilities of occurrence of AAI is at least an order of magnitude lower, no such relationship exists (Fig. 10). Our model results thus suggest that the enhanced viscous energy dissipation above the rough topography is associated with greater AAI there.

Away from the shallow end of the slope, the occurrence of AAI above the rough topography in the CE rough-topography experiment is relatively sporadic and much less frequent than those in the AE rough-topography experiments (Fig. 9b). In fact, energy dissipation rate (Fig. 7b) and ageostrophic kinetic energy (Fig. 8b) in the slope region in the CE rough-topography experiment are also generally weaker than those in the AE rough-topography experiments. We attribute this result to the weaker near-bottom eddy velocities during the westward evolution of a CE, while, in contrast, the AE tends to maintain its deep structure and its near-bottom velocities (Figs. 11a-c).

Recent work on LOB near sloping topographic boundaries considers submesoscale generation via symmetric instability and inertial instability (e.g., Wenegrat et al. 2018; Naveira-Garabato et al. 2019). For example, Naveira-Garabato et al. (2019) showed that topographic frictional stress acting on an abyssal boundary current tilts isopycnals towards the vertical and compresses them horizontally. The boundary current subsequently develops inertial and symmetric instabilities when the lateral stratification and shear become sufficiently large. However, Table 2 shows that conditions for these instabilities are rarely satisfied in our model. This may be due to the relatively small Rossby number in our experiments which prevents PV_Z from becoming negative. Although PV_H is a negative definite quantity for geostrophic flow (Thomas et al. 2013), there are no large negative values of PV_H near the bottom slope to overcome positive PV_Z (not shown). Furthermore, we found that the bottom Richardson number in our model simulations is often larger than what is required for SI and INI to be the dominant modes of instability, according to the regime diagram of Wenegrat et al. (2018). The probabilities of SI and INI are higher in the rough-topography experiments than in the smooth-topography experiments due possibly to weaker bottom stratification above the rough topography (Wenegrat et al. 2018), but they are still more than an order of magnitude smaller than the probability of AAI.

AAI can arise through a shear-assisted resonance of at least one unbalanced wave (inertial gravity wave or Kelvin wave) with coincident Doppler-shifted phase speeds (McWilliams et al. 2004), and wave-wave interaction provides a mechanism of direct energy transfer toward small-scales, without a turbulent cascade process, thus enhancing the viscous dissipation (Staquet and Sommeria 2002). AAI has been identified in several previous studies (see e.g. Wang et al. 2012 and references therein) and these studies show that significant ageostrophic growth rates can occur in the neighborhood of $A-|S|=0$. Even though the maximum growth rates of these ageostrophic modes are smaller than that of the classical geostrophic mode (baroclinic instability), it is important to note that the geostrophic mode is only unstable at length scales larger than the first baroclinic deformation radius which is far from the turbulent dissipation scale, and that at smaller scales the ageostrophic mode is the only unstable one (Müller et al. 2005). Different from other LOB instabilities, the criteria for AAI can be satisfied even if the magnitude of Rossby number is moderate, and is therefore considered to be one possible route to dissipation for the large-scale ocean general circulation (Wang et al. 2012).

3.2. Experiments with a sea of random eddies

In the experiments initialized with a sea of random eddies, the eddies again propagate predominately westward while at the same time interacting with each other through shear deformation and merging of eddies of the same polarity. As expected, the total eddy energy decreases with time, and at the end of model simulation on day 300, only some relatively weak eddies (with maximum amplitude of about 6 cm) can be found near the shelf.

Fig. 12 shows the diagnosed energy budget in the high-resolution box region near the western boundary for both the control and rough-topography experiments. The energy budget is again closed, and the main balance, similar to that in the single eddy experiments, is between changes of total energy within the box, energy flux into the box and dissipation of energy within the box by bottom drag and viscous friction, with diffusive energy flux making a negligible contribution. The cumulative energy dissipation by day 300 in the rough-topography experiment is 2.5×10^{14} J comparing to the 2.1×10^{14} J in the control experiment, representing an enhancement of about 20%.

The presence of rough topography also profoundly changes the relative importance of energy dissipation by bottom drag and interior viscous dissipation (Fig. 13). In the control experiment, bottom frictional dissipation is most important, accounting for about 46% of the total energy dissipation. In contrast, bottom dissipation is least important in the rough-topography experiment, accounting for less than 14% of the total dissipation. Including rough topography on the continental slope reduces the time- and volume-integrated bottom dissipation by about two-thirds (6.7×10^{13} J in control vs. 2.4×10^{13} J in rough-topography), but almost doubles the total amount of interior viscous dissipation. While there is only a moderate enhancement in vertical viscous energy dissipation (6.0×10^{13} J in control vs. 7.1×10^{13} J in rough-topography), the time- and volume-integrated horizontal viscous dissipation is almost quadrupled (1.9×10^{13} J in control vs. 7.7×10^{13} J in rough-topography), which leads to an overall increase in energy dissipation in the rough-topography experiment by about 20%.

Furthermore, differences in energy dissipation rate between the control and rough-topography experiments become significant only after the eddies have come into contact with the upper slope. Fig. 14 shows the volume-normalised and volume-integrated energy dissipation rates as a function of depth during day 121-300. In both experiments, large energy dissipation rates are concentrated in the upper 1500 m or so where the energy dissipation rate is almost doubled when the rough topography is present. At depths greater than 1500 m, energy dissipation rates in both the control and rough-topography experiments, as well as their differences, are relatively small. This result highlights the importance of the western boundary in dissipating eddy energy. Recall that rough topography is added on the slope over the full depth range from roughly 3000 m at the ocean bottom to the continental shelf. The key role of the western boundary here is that its presence brings the (rough) topography up in the water column such that the seabed is in direct contact with the energetic upper part of the eddies.

There is again co-variation between the probabilities of occurrence of AAI and magnitude of viscous dissipation in the rough-topography experiment, but not in the control experiment where the probability of AAI is about two orders of magnitude lower (Figs. 13d-e). Fig. 15 shows the along slope mean dissipation rate, ageostrophic kinetic energy and probabilities of occurrence of AAI during day 201-240 in experiments with a sea of random eddies. The results are very similar to those in the single eddy experiments: in the rough-topography experiment, there are distinct bands of enhanced energy dissipation rates, elevated ageostrophic kinetic energy and greater probabilities of AAI, all occurring right above the rough topography along the slope. Results from other time periods (e.g., day 121-160, day 161-200, day 241-280) are very similar.

4. Discussion

4.1 Lee wave energy dissipation

Our study shows that the enhanced eddy energy dissipation near the western boundary in the experiments with a rough topography is associated with greater AAI. On the other hand, internal lee wave generation as a result of eddy geostrophic flow impinging on rough, small-scale topography is thought to be an important route to eddy energy dissipation, particularly in the Southern Ocean (Nikurashin and Ferrari 2010b; Nikurashin et al. 2013). Here we explore the role of lee wave generation in the enhanced dissipation found in our rough-topography experiments.

Following Nagai et al. (2015) and Shakespeare and Hogg (2017b), we apply a Lagrangian filter to separate the model flow field into the (internal) wave and nonwave components, with the wave component defined as motions with Lagrangian frequencies exceeding the local inertial frequency. The advantage of the Lagrangian filtering method is that it accounts for the Doppler shifting of wave frequency associated with stationary waves such as lee waves. Over 60 million flow-following particles (one particle at every model grid point) are introduced in the high-resolution region of the two single AE experiments (control and rough) and their trajectories are computed every hour over a 1-week analysis period (model day 82-88). The model velocities are then interpolated from the model grid to the particle trajectories where a high-pass filter is applied to isolate the wave field. After that, the high-pass filtered velocities are interpolated back from the particle locations to the model grid. Following Shakespeare and Hogg (2018), we performed an evaluation of errors associated with forward and backward interpolations between the model grid and particle locations and found that the errors associated with inhomogeneity of particle concentrations are generally negligible (not shown). To avoid the ringing effect associated with the high-pass filtering at the beginning and end of the 1-week period, only the middle 5 days of the filtered velocity data are used to calculate the wave energy dissipation (ε_W) and the nonwave energy dissipation (ε_{NW}):

$$\begin{aligned} \varepsilon_W &= A_h\left[\left(\frac{\partial \mathbf{u}_H}{\partial x}\right)^2+\left(\frac{\partial \mathbf{u}_H}{\partial y}\right)^2\right]+A_z\left(\frac{\partial \mathbf{u}_H}{\partial z}\right)^2 \\ \varepsilon_{NW} &= A_h\left[\left(\frac{\partial \mathbf{u}_L}{\partial x}\right)^2+\left(\frac{\partial \mathbf{u}_L}{\partial y}\right)^2\right]+A_z\left(\frac{\partial \mathbf{u}_L}{\partial z}\right)^2 \end{aligned}, \quad (6)$$

where $\mathbf{u}_H$ is the high frequency velocity associated with wave motions and $\mathbf{u}_L$ is the low frequency velocity associated with nonwave motions. A_h and A_z are the horizontal and vertical viscosities, respectively.

Fig. 16 shows the results from the AE control and AE rough experiments. In the control experiment, the nonwave energy dissipation dominates and is concentrated mostly in the upper 1000 m, with wave energy dissipation making a very small contribution near the shallow end of the slope (Figs. 16a-b). The domain-integrated nonwave energy dissipation is more than one order of magnitude larger than the wave energy dissipation.

In the rough-topography experiment, although the nonwave dissipation is still the leading energy dissipation term, there are some noticeable differences. First, both wave and nonwave energy dissipation rates are strongly enhanced in a band right above the rough topography along the slope (Figs. 16c-d). Second, the ratio between the domain-integrated nonwave and wave energy dissipation is reduced to only slightly over two. This result shows that direct energy dissipation of lee waves contributes to the bottom-enhanced dissipation seen in the rough-topography experiments. Furthermore, we find that the horizontal strain rates are significantly greater when AAI occurs. This increase in strain rate may be in part associated with internal lee wave generation as a result of eddy-topography interaction. The possible role of lee wave generation in triggering AAI at the western boundary or in the Southern Ocean is intriguing but is left for a future study.

4.2 Non-propagating form drag

According to the linear theory, freely propagating internal lee waves are only generated by topographic features with horizontal wavenumbers greater than f/u_0, where f is the Coriolis frequency and u_0 is the bottom mean flow speed, while the response to larger-scale topography is evanescent, i.e., non-propagating, and results in no drag or energy loss of the mean flow. The linear theory requires the inverse topographic Froude number Nh/u_0 to be small, where N is the bottom buoyancy frequency and h is the topographic height. However, recent work by Klymak (2018) suggests that for a variety of topographic regimes, $Nh/u_0 > 1$, indicating the flow is significantly nonlinear and dissipative, and that the non-propagating form drag is likely to be more important for energy dissipation than propagating lee waves. In the rough-topography experiments, the root-mean-squared height of the synthesized rough topography h = 190 m, N is about 6e-3 s^{-1} up the slope and 1e-3 s^{-1} down the slope, and the bottom velocity u_0 is about 0.1 m s^{-1} up the slope and about 0.05 m s^{-1} down the slope, so the inverse Froude number Nh/u_0 is about 4-11. This means the bottom flow is nonlinear and dissipative, and the non-propagating form drag effect is likely to be present in our model experiments (Klymak 2018). Note that the contribution of non-propagating form drag to eddy energy dissipation is included in the nonwave energy dissipation term (Figs. 16b and d).

4.3 Arrested topographic waves

Dewar and Hogg (2010) showed that when an anticyclonic eddy impinges on a western wall, boundary Kelvin waves excited poleward of the eddy can be arrested by the opposing eddy current.

Energy can then be transferred from the balanced eddy flow to unbalanced Kelvin waves which results in exponential growth of wave disturbance and decay of eddy energy. At the western boundary, only anticyclonic eddies are able to arrest boundary Kelvin waves; Kelvin waves excited by cyclonic eddies impinging on the western wall are free to propagate equatorward. Therefore, if the arrested boundary/topographic waves were responsible for dissipating eddy energy in our experiments, we would expect to see large differences between single AE and CE experiments. Figs. 5-7 show that there are no qualitative differences in the magnitude and spatial pattern of eddy energy dissipation in single AE and CE experiments, with either smooth or rough topography. The relative insignificance of the arrested boundary/topographic waves in our experiments may be related to weak bottom eddy velocities and/or the sloping topography (rather than a vertical wall) that the eddies encounter.

4.4 Non-hydrostatic effect

The radiating internal waves from topography with horizontal scales in the range from $|f/u_0|$ to N/u_0, typically span wavelengths from about O (0.1) km to O (10) km (Bell 1975a,b). In order to resolve these small-scale topography and internal wave motions, we have used a high spatial resolution, which is 20 m in the vertical and variable in the horizontal with a finest grid of 400 m in the slope region (Fig. 1). Furthermore, the non-hydrostatic configuration is used in all model simulations. Under such configuration, the model is very expensive to run. To test the model's sensitivity to hydrostatic approximation, we re-run the rough-topography experiment with a sea of random eddies from day 161 to 200 with hydrostatic approximation (other configurations remain the same). It is worth pointing out that the hydrostatic model is about 2 times faster to run than the non-hydrostatic model. Fig. 17 shows that the difference between the results of the hydrostatic and non-hydrostatic models is very small. For example, the time-integrated total energy dissipation is

2.769×10^{13} J and 2.766×10^{13} J in the hydrostatic and non-hydrostatic models, respectively. This result is potentially useful for future studies that plan to employ a similar model setup. The non-hydrostatic effects on the ageostrophic instabilities can, however, be significant when the stratification is weak (e.g. Molemaker et al. 2005).

5. Summary

In this study we have investigated the energetics of eddy-western boundary interaction in a high-resolution idealized ocean model, motivated by a recent study that highlights the western boundary acts as a 'graveyard' for westward-propagating ocean eddies. We initialize the idealized model with either a single eddy or a sea of random eddies, and run it with both smooth topography and synthetically-generated rough topography. We find significant dissipation of incident eddy energy at the western boundary, regardless of whether the model topography at the western boundary is smooth or rough. We attribute it to the fact that bottom topography (rough or not) is brought upwards to the surface at the western boundary and as such it comes into contact with the energetic part of the eddies in the upper water column, whereas in the open ocean the eddy bottom velocities that interact with the bottom topography are much weaker.

The presence of rough topography, on the other hand, leads to enhanced eddy energy dissipation rates, and, perhaps more importantly, changes the relative importance of energy dissipation by bottom drag and interior viscous dissipation. The leading process for removing eddy energy switches from bottom frictional drag in model experiments with a smooth topography to interior viscous dissipation in experiments where rough topography is added. Whether eddy energy is removed from the ocean by bottom frictional drag or by interior viscous dissipation is an important matter since energy dissipation by bottom friction is an adiabatic process, while that by interior viscous dissipation may lead to bottom-enhanced diapycnal mixing in the western boundary region. Recent sensitivity experiments show that the stratification and overturning circulation in ocean general circulation models are very sensitive to the magnitude and structure of the eddy-induced mixing at the western boundary (Saenko et al. 2012).

In our model experiments, there appears to be a close connection between small-scale energy dissipation and ageostrophic motions which prompts us to examine conditions for loss of balance. We find that except for anticyclonic-ageostrophic instability or AAI in the rough-topography experiments, conditions for other types of loss of balance are rarely satisfied. In all rough-topography experiments, there is a close spatial and temporal correspondence between the probabilities of occurrence of AAI and the magnitude of interior viscous energy dissipation rate, whereas in the smooth-topography experiments where the probabilities of occurrence of AAI is at least an order of magnitude lower, no such relationship exists. Our model results thus suggest that the enhanced viscous energy dissipation above the rough topography in the rough-topography experiments is associated with greater AAI there. It is possible that the enhanced AAI in the rough-topography experiments is a result of lee wave generation and non-propagating form drag effect and that AAI simply acts to facilitate the breaking of these bottom-generated wave structures. The relationship between AAI and lee wave breaking in both its propagating and non-propagating forms is clearly worthy of further investigation and is left for a future study.

Finally, results from this study have implications for the recently-proposed energetically-consistent mesoscale eddy parameterization schemes which require solving an explicit eddy energy budget to control the magnitude of eddy transfer coefficients (Eden and Greatbatch 2008; Marshall and Adcroft 2010; Marshall et al. 2012; Jansen and Held 2014; Jansen et al. 2015; Mak et al. 2018). One of the key unknowns in this eddy energy budget is eddy energy dissipation rate and its spatial structure (Mak et al. 2018). We suggest that the eddy graveyard at the western boundary of ocean basins may play a significant role.

Acknowledgements. ZY thanks John A. Goff for his help with the synthetically-generated rough topography and also thanks Zhengguang Zhang for sharing the Argo-composite data used in this study. ZY is supported by a scholarship from the Chinese Scholarship Council and the Natural Natural Science Foundation of China (41811530301, 41976003, 911821160). This paper is part of ZY's doctoral dissertation at Hohai University and ZY would like to thank Hohai University for its support. XZ acknowledges support by a Royal Society International Exchanges Award (IEC\NSFC\170007). XZ and DPM acknowledge partial support from the UK Natural Environmental Research Council, NE/R000999/1. GW is supported by the Program of Shanghai Academic/Technology Research Leader (17XD1400600). The research presented in this paper was carried out on the High Performance Computing Cluster supported by the Research and Specialist Computing Support service at the University of East Anglia.

APPENDIX

Derivation of the Energy Equations

a. Kinetic energy

The momentum equations in the x and y directions are

$$\frac{\partial u}{\partial t} + \nabla \cdot (u\mathbf{u}) - fv = -\frac{1}{\rho_0}\frac{\partial}{\partial x} p^* + D_u, \text{ and} \tag{A1}$$

$$\frac{\partial v}{\partial t} + \nabla \cdot (v\mathbf{u}) + fu = -\frac{1}{\rho_0}\frac{\partial}{\partial y} p^* + D_v, \tag{A2}$$

where

$$D_u = \left(\frac{\partial}{\partial x} A_h \frac{\partial u}{\partial x} + \frac{\partial}{\partial y} A_h \frac{\partial u}{\partial y}\right) + \frac{\partial}{\partial z} A_z \frac{\partial u}{\partial z} + C_b \cdot |\mathbf{u}| \cdot u, \text{ and}$$

$$D_v = \left(\frac{\partial}{\partial x} A_h \frac{\partial v}{\partial x} + \frac{\partial}{\partial y} A_h \frac{\partial v}{\partial y}\right) + \frac{\partial}{\partial z} A_z \frac{\partial v}{\partial z} + C_b \cdot |\mathbf{u}| \cdot v, \tag{A3}$$

include viscous terms and bottom friction. The term $p^* = \int_z^{\eta} \rho^* g dz + p_{NH}$ is the reference pressure with reference density $\rho^* = \rho - \rho_{ref}$ and non-hydrostatic pressure term p_{NH}, ρ_{ref} is the background density. $\nabla\cdot$ is the divergence operator. **u** is the three-dimensional velocity vector.

Multiplying Eqs. (A1) and (A2) by *u* and *v*, respectively and adding them together, we obtain the equation for kinetic energy:

$$\frac{\partial KE}{\partial t} = -\nabla \cdot F - \varepsilon - D_b - \frac{\rho^* g w}{\rho_0}, \tag{A4}$$

where $KE = \frac{1}{2}\left(u^2 + v^2\right)$ is the kinetic energy, *F* is the kinetic energy flux term, $\varepsilon = A_h\left[(\frac{\partial \mathbf{u}}{\partial x})^2 + (\frac{\partial \mathbf{u}}{\partial y})^2\right] + A_z\left(\frac{\partial \mathbf{u}}{\partial z}\right)^2$ is viscous energy dissipation, D_b is bottom frictional dissipation, $\frac{\rho^* g w}{\rho_0}$ is the conversion term between kinetic energy and potential energy.

b. Available potential energy

To derive the equation for available potential energy (APE), we start with the equation of density,

$$\frac{\partial \rho}{\partial t} + \nabla \cdot (\mathbf{u}\rho) = K_\rho, \tag{A5}$$

where $K_\rho = \left(\frac{\partial}{\partial x} K_h \frac{\partial \rho}{\partial x} + \frac{\partial}{\partial y} K_h \frac{\partial \rho}{\partial y} \right) + \frac{\partial}{\partial z} K_z \frac{\partial \rho}{\partial z}$ is the diffusion term.

There are several ways of defining the APE (Huang 2005) and here we choose the one that is analogous to the quasigeostrophic definition which is widely used (e.g., Pedlosky 1987; Oort et al. 1989, 1994; Huang 2010; von Storch et al. 2012). Note that this definition assumes the variation of stratification is much smaller than the background stratification, in order to neglect the vertical advection of perturbed density.

We define $APE = -\frac{1}{2}\frac{g}{n_0}\rho^{*2}$, with $n_0 = \rho_0 \frac{d\rho_{ref}}{dz}$.

The conservation equation for APE is then obtained by multiplying Eq. (A5) by $-\frac{1}{2}\frac{g}{n_0}\rho^*$:

$$\frac{\partial APE}{\partial t} = -\nabla \cdot \mathbf{u}APE + K_{APE} + \frac{\rho^* g w}{\rho_0}, \tag{A6}$$

where K_{APE} is the diffusion term.

REFERENCES

Alford, M. H., A. Y. Shcherbina, and M. C. Gregg, 2013: Observations of near-inertial gravity waves radiating from a frontal jet. J. Phys. Oceanogr., 43, 1225–1239, https://doi:10.1175/JPO-D-12-0146.1.

Arbic, B. K., and Coauthors, 2009: Estimates of bottom flows and bottom boundary layer dissipation of the oceanic general circulation from global high-resolution models. J. Geophys. Res., 114, C02024, https://doi:10.1029/2008JC005072.

Bell, T., 1975a: Lee waves in stratified flows with simple harmonic time dependence. J. Fluid Mech., 67, 705–722, https://doi.org/ 10.1017/S0022112075000560.

——, 1975b: Topographically generated internal waves in the open ocean. J. Geophys. Res., 80, 320–327, https://doi.org/10.1029/ JC080i003p00320.

Brannigan, L., D. P. Marshall, A. C. N. Garabato, and A. J. G. Nurser, 2015: The seasonal cycle of submesoscale flows. Ocean Modell., 92, 69–84, https://doi:10.1016/j.ocemod.2015.05.002.

Chelton, D. B., M. G. Schlax, R. M. Samelson, and R. A. de Szoeke, 2007: Global observations of large oceanic eddies. Geophys. Res. Lett., 34, L15606, https://doi.org/10.1029/2007GL030812.

Clément, L., E. Frajka-Williams, K. Sheen, J. Brearley, and A. N. Garabato, 2016: Generation of internal waves by eddies impinging on the western boundary of the North Atlantic. J. Phys. Oceanogr., 46, 1067–1079, https://doi.org/10.1175/JPO-D-14-0241.1.

Dewar, W. K., and A. M. Hogg, 2010: Topographic inviscid dissipation of balanced flow. Ocean Modell., 32, 1–13, https://doi:10.1016/ j.ocemod.2009.03.007.

Duhaut, T. H., and D. N. Straub, 2006: Wind stress dependence on ocean surface velocity: Implications for mechanical energy input to ocean circulation. J. Phys. Oceanogr., 36, 202–211, https://doi:10.1175/JPO2842.1.

Eden, C., and R. J. Greatbatch, 2008: Diapycnal mixing by mesoscale eddies. Ocean Modell., 23, 113–120, https://doi:10.1016/ j.ocemod.2008.04.006.

Ferrari, R., and C. Wunsch, 2009: Ocean circulation kinetic energy: Reservoirs, sources, and sinks. Annu. Rev. Fluid Mech., 41, 253– 282, https://doi.org/10.1146/annurev.fluid.40.111406.102139.

Gill, A. E., J. Green, and A. J. Simmons, 1974: Energy partition in large-scale ocean circulation and production of mid-ocean eddies. Deep-Sea Res. Oceanogr. Abstr., 21, 499–528, https:// doi.org/10.1016/0011-7471(74)90010-2.

Goff, J. A., and T. H. Jordan, 1988: Stochastic modeling of seafloor morphology: Inversion of sea beam data for second-order statistics. J. Geophys. Res., 93, 13 589–13 608, https://doi.org/ 10.1029/JB093iB11p13589.

Huang, R. X., 2005: Available potential energy in the world’s oceans. J. Mar. Res., 63, 141–158, https://doi.org/10.1357/ 0022240053693770.

——, 2010: Ocean Circulation: Wind-Driven and Thermohaline Processes. Cambridge University Press, 806 pp.

Hughes, C. W., and C. Wilson, 2008: Wind work on the geostrophic ocean circulation: An observational study of the effect of small scales in the wind stress. J. Geophys. Res., 113, C02016, https:// doi.org/10.1029/2007JC004371.

Jansen, M. F., and I. M. Held, 2014: Parameterizing subgrid-scale eddy effects using energetically consistent backscatter. Ocean Modell., 80, 36–48, https://doi.org/10.1016/j.ocemod.2014.06.002.

——, A. J. Adcroft, R. Hallberg, and I. M. Held, 2015: Parameterization of eddy fluxes based on a mesoscale energy budget. Ocean Modell., 92, 28–41, https://doi.org/10.1016/ j.ocemod.2015.05.007.

Klymak J M., 2018: Nonpropagating Form Drag and Turbulence due to Stratified Flow over Large-Scale Abyssal Hill Topography. J. Phys. Oceanogr., 48, 2383–2395, https://doi.org/10.1175/JPO-D-17-0225.1

Large, W. G., J. C. McWilliams, and S. C. Doney, 1994: Oceanic vertical mixing: A review and a model with a nonlocal boundary layer parameterization. Rev. Geophys., 32, 363–403, https://doi.org/10.1029/94RG01872.

Lee, D., and P. Niiler, 1998: The inertial chimney: The near-inertial energy drainage from the ocean surface to the deep layer. J. Geophys. Res., 103, 7579–7591, https://doi.org/10.1029/ 97JC03200.

Mak, J. R. Maddison, D. P. Marshall, and D. R. Munday, 2018: Implementation of a geometrically informed and energetically constrained mesoscale eddy parameterization in an ocean circulation model. J. Phys. Oceanogr., 48, 2363–2382, https://doi.org/10.1175/JPO-D-18-0017.1.

Marshall, D. P., and A. J. Adcroft, 2010: Parameterization of ocean eddies: Potential vorticity mixing, energetics and Arnold's first stability theorem. Ocean Modell., 32, 188–204, https://doi.org/ 10.1016/j.ocemod.2010.02.001.

——, J. R. Maddison, and P. S. Berloff, 2012: A framework for parameterizing eddy potential vorticity fluxes. J. Phys. Oceanogr., 42, 539–557, https://doi.org/10.1175/JPO-D-11-048.1.

Marshall, J., A. Adcroft, C. Hill, L. Perelman, and C. Heisey, 1997: A finite-volume, incompressible Navier-Stokes model for studies of the ocean on parallel computers. J. Geophys. Res., 102, 5753–5766, https://doi.org/10.1029/96JC02775.

McWilliams, J. C., 2003: Diagnostic force balance and its limits. Nonlinear Processes in Geophysical Fluid Dynamics, O. V. Fuentes, J. Sheinbaum, and J. Ochoa, Eds., Kluwer, 287–304.

——, M. J. Molemaker, and I. Yavneh, 2004: Ageostrophic, anticyclonic instability of a geostrophic, barotropic boundary current. Phys. Fluids, 16, 3720–3725, https://doi:10.1063/1.1785132.

——, and I. Yavneh, 1998: Fluctuation growth and instability associated with a singularity in the balanced equations. Phys. Fluids, 10, 2587–2596, https://doi:10.1063/1.869772.

Molemaker, M. J., J. C. McWilliams, and I. Yavneh, 2005: Baroclinic instability and loss of balance. J. Phys. Oceanogr., 35, 1505–1517, https://doi:10.1175/JPO2770.1.

Müller, P., J. C. McWilliams, and M. J. Molemaker, 2005: Routes to dissipation in the ocean: The 2D/3D turbulence conundrum. Marine Turbulence, H. B. J. Simpson and J. Sündermann, Eds., Cambridge University Press, 397–405.

Nagai, T., A. Tandon, E. Kunze, and A.Mahadevan, 2015: Spontaneous generation of near-inertial waves by the Kuroshio Front. J. Phys.Oceanogr., 45, 2381–2406, https://doi:10.1175/JPO-D-14-0086.1.

Naveira Garabato, A. C., and Coauthors, 2019: Rapid mixing and exchange of deep-ocean waters in an abyssal boundary current. Proc. Natl. Acad. Sci. U. S. A., 116, 13233–13238, https://doi.org/10.1073/pnas.1904087116.

Nikurashin, M., and R. Ferrari, 2010a: Radiation and dissipation of internal waves generated by geostrophic flows impinging on small-scale topography: Theory. J. Phys. Oceanogr., 40, 1055– 1074, https://doi.org/10.1175/2009JPO4199.1.

——, and ——, 2010b: Radiation and dissipation of internal waves generated by geostrophic flows impinging on small-scale topography: Application to the Southern Ocean. J. Phys. Oceanogr., 40, 2025–2042, https://doi.org/10.1175/2010JPO4315.1.

——, G. K. Vallis, and A. Adcroft, 2013: Routes to energy dissipation for geostrophic flows in the Southern Ocean. Nat. Geosci., 6, 48–51, https://doi.org/10.1038/ngeo1657.

Oort, A., S. Ascher, S. Levitus, and J. Peixóto, 1989: New estimates of the available potential energy in the World Ocean. J. Geophys. Res., 94, 3187–3200, https://doi:10.1029/JC094iC03p03187.

——, L. Anderson, and J. Peixóto, 1994: Estimates of the energy cycle of the oceans. J. Geophys. Res., 99, 7665–7688, https://doi:10.1029/93JC03556.

Pedlosky, J., 1987: Geophysical Fluid Dynamics. Springer-Verlag, 710 pp.

Saenko, O., X. Zhai, W. Merryfield, and W. Lee, 2012: The combined effect of tidally and eddy-driven diapycnal mixing on the large-scale ocean circulation. J. Phys. Oceanogr., 42, 526–538, https://doi.org/10.1175/JPO-D-11-0122.1.

Sen, A., R. B. Scott, and B. K. Arbic, 2008: Global energy dissipation rate of deep-ocean low-frequency flows by quadratic bottom boundary layer drag: Computations from current-meter data. Geophys. Res. Lett., 35, L09606, https://doi.org/10.1029/ 2008GL033407.

Shakespeare, C. J., and A. M. Hogg, 2017a: The viscous lee wave problem and its implications for ocean modelling. Ocean Modell., 113, 22–29, https://doi.org/10.1016/j.ocemod.2017.03.006.

——, and ——, 2017b: Spontaneous surface generation and interior amplifification of internal waves in a regional-scale ocean model. J. Phys. Oceanogr., 47, 811–826, https://doi.org/10.1175/JPO-D-16-0188.1.

——, and ——, 2018: The life cycle of spontaneously generated internal waves. J. Phys. Oceanogr., 48, 343–359, https://doi.org/10.1175/JPO-D-17-0153.1

Staquet, C., and J. Sommeria, 2002: Internal gravity waves: From instabilities to turbulence. Annu. Rev. Fluid Mech., 34, 559– 593, https://doi:10.1146/annurev.fluid.34.090601.130953.

Stöber, U., M. Walter, C. Mertens, and M. Rhein, 2008: Mixing estimates from hydrographic measurements in the deep western boundary current of the North Atlantic. Deep-Sea Res. I, 55, 721–736, https://doi:10.1016/j.dsr.2008.03.006.

Teague, W. J., M. J. Carron, and P. J. Hogan, 1990: A comparison between the generalized digital environmental model and Levitus climatologies. J. Geophys. Res., 95, 7167–7183, https://doi:10.1029/JC095iC05p07167.

Thomas, L., J. Taylor, R. Ferrari, and T. Joyce, 2013: Symmetric in□stability in the Gulf Stream. Deep-Sea Res., 91, 96–110, https://doi:10.1016/j.dsr2.2013.02.025.

von Storch, J. S., C. Eden, I. Fast, H. Haak, D. Hernández-Deckers, E. Maier-Reimer, J. Marotzke, and D. Stammer, 2012: An estimate of the Lorenz energy cycle for the world ocean based on the 1/108 STORM/NCEP simulation. J. Phys. Oceanogr., 42, 2185–2205, https://doi:10.1175/JPO-D-12-079.1.

Wang, P., J. McWilliams, and Z. Kizner, 2012: Ageostrophic instability in rotating shallow water. J. Fluid Mech., 712, 327– 353, https://doi:10.1017/jfm.2012.422.

Wang, Y., and A. L. Stewart, 2018: Eddy dynamics over continental slopes under retrograde winds: Insights from a model inter-comparison. Ocean Modell., 121, 1–18, https:// doi.org/10.1016/j.ocemod.2017.11.006.

Walter, M., C. Mertens, and M. Rhein, 2005: Mixing estimates from a large-scale hydro-graphic survey in the North Atlantic. Geophys. Res. Lett., 32, L13605, https://doi.org/10.1029/ 2005GL022471.

Wenegrat, J. O., J. Callies, and L. N. Thomas, 2018: Submesoscale baroclinic instability in the bottom boundary layer. J. Phys. Oceanogr., 48, 2571–2592, https://doi.org/10.1175/JPO-D-17-0264.1.

Williams, P. D., T. W. Haine, and P. L. Read, 2008: Inertia–gravity waves emitted from balanced flow: Observations, properties, and consequences. J. Atmos. Sci., 65, 3543–3556, https://doi.org/ 10.1175/2008JAS2480.1.

Wunsch, C., 1998: The work done by the wind on the oceanic general circulation. J. Phys. Oceanogr., 28, 2332–2340, https://doi.org/ 10.1175/1520-0485(1998)028,2332:TWDBTW.2.0.CO;2.

Xu, C., X. Zhai, and X.-D. Shang, 2016: Work done by atmospheric winds on mesoscale ocean eddies. Geophys. Res. Lett., 43, 12 174–12 180, https://doi.org/10.1002/2016GL071275.

Zhang, Z., Y. Zhang, W. Wang, and R. X. Huang, 2013: Universal structure of mesoscale eddies in the ocean. Geophys. Res. Lett., 40, 3677–3681, https://doi:10.1002/grl.50736.

Zhai, X., and D. P. Marshall, 2013: Vertical eddy energy fluxes in the North Atlantic subtropical and subpolar gyres. J. Phys. Oceanogr., 43, 95–103, https://doi.org/10.1175/ JPO-D-12-021.1.

——, H. L. Johnson, and D. P. Marshall, 2010: Significant sink of ocean-eddy energy near western boundaries. Nat. Geosci., 3, 608–612, https://doi.org/10.1038/ngeo943.

——, ——, ——, and C. Wunsch, 2012: On the wind power input to the ocean general circulation. J. Phys. Oceanogr., 42, 1357–1365, https://doi.org/10.1175/JPOD-12-09.1.

——, and R. J. Greatbatch, 2007: Wind work in a model of the northwest Atlantic Ocean. Geophys. Res. Lett., 34, L04606, https://doi:10.1029/2006GL028907.

List of tables

List of figures

Fig. 1. The model domain for single eddy experiments with sponge layers at the southern, eastern and northern boundaries (gray shading). The spatially variable grid resolution in both horizontal directions is shown in the two side panels. The white contours represent the isobaths (m) of the smooth topography. The region near the western boundary inside the gray box is where the eddy energy budget analysis is conducted. The color shading in the main panel shows the SSH (cm) on day 1 in the experiment initialized with an anticyclonic eddy. The model domain for the experiment with a sea of random eddies is the same except that it is wider (717 km) in the zonal direction.

Fig. 2. Topography used in (a) control and (b) rough-topography experiments. The color shading in (a) shows the background temperature (^{o}C) in the control experiment initialized with an anticyclonic eddy. The color shading in (b) shows the bathymetry (km) in the rough-topography experiment.

Fig. 3. SSH (cm) fields on day 1 in experiments initialized with (a) a single AE, (b) a single CE and (c) a sea of random eddies. Gray lines represent the isobaths (m) of the smooth topography.

Fig. 4. Eddy (a) trajectories and (b) amplitudes in the control (solid), rough 1 (dashed) and rough 2 (dotted) experiments initialized with either a single AE (red) or CE (blue). Gray contours in (a) show the isobaths (m) of the smooth topography and the black box encloses the high-resolution (400 m) region where the synthetically-generated rough topography is added to the smooth hyperbolic tangent function in the rough-topography experiments. The blue and red dots with black circles in (a) and (b) indicate the eddy locations and amplitudes every 40 days.

Fig. 5. Time series of cumulative energy flux into the gray box near the western boundary in

Fig. 1 (black solid), cumulative energy dissipation within the box (blue), cumulative diffusive energy flux across the boundaries of the box (green), total energy within the box (red) and the residue (black dashed) for the five single eddy experiments.

Fig. 6. Instantaneous bottom frictional dissipation and interior viscous dissipation in five single eddy experiments. The upper panels are for the CE experiments and lower panels for the AE experiments. Solid, dashed and dotted curves represent results from the control, rough 1 and rough 2 experiments, respectively.

Fig. 7. Along slope mean dissipation rate (unit: J) integrated during day 81-120 in single eddy experiments. (a) and (b) are for the CE control and rough-topography experiments, respectively. (c) is ratio between (a) and (b), i.e., (b) divided by (a), and the black lines in (c) are contours of ten; (d-f) are the same as (a-c) but for the AE control and AE rough 1 experiments; (g-h) are the same as (b-c) but for the AE rough 2 experiment.

Fig. 8. Along slope mean ageostrophic kinetic energy (unit: J) integrated during day 81-120 in single eddy experiments. (a) and (b) are for the CE control and rough-topography experiments, respectively. (c) is the ratio between (a) and (b), i.e., (b) divided by (a), and the black lines in (c) are contours of ten; (d-f) are the same as (a-c) but for the AE control and AE rough 1 experiments; (g-h) are the same as (b-c) but for the AE rough 2 experiment.

Fig. 9. Along slope mean probabilities of occurrence of AAI during day 81-120. (a) CE control; (b) CE rough; (c) AE control; (d) AE rough 1; (e) AE rough 2.

Fig. 10. Time series of occurrence of AAI (black) and viscous energy dissipation (blue; watt) during day 81-120 in the five single eddy experiments.

Fig. 11. Along slope mean kinetic energy (J) during day 81-120 in single eddy experiments. Only kinetic energy with values within the colorbar range limits is shown.

Fig. 12. Time series of cumulative energy flux into the gray box near the western boundary in Fig. 1 (black solid), cumulative energy dissipation within the box (blue), cumulative diffusive energy flux across the boundaries of the box (green), total energy within the box (red) and the residue (black dashed) for the experiments initialized with a sea of random eddies.

Fig. 13. Instantaneous (a) bottom frictional dissipation, (b) horizontal viscous dissipation, (c) vertical viscous dissipation and (d-e) relationship between energy dissipation and probabilities of occurrence of AAI in the two experiments initialized with a sea of random eddies; and the relationship between dissipation (unit: watt) and AAI (percent) for (d) control case; (e) rough case.

Fig. 14. (a) Volume-normalised and (b) volume-integrated energy dissipation rates as a function of depth during day 121-300 in the sea of random eddies experiments. Blue (red) line shows the result from the experiment with a smooth (rough) topography, and the color shading represents the standard deviation.

Fig. 15. Along slope mean dissipation rate (a-c; unit: J), ageostrophic kinetic energy (d-f; unit: J) and probabilities of occurrence of AAI (g-h) integrated over day 201-240 in the sea of random eddies experiments. Black lines in c & f represent contours of ten.

Fig. 16. The time- (day 83-87) and volume-integrated wave (ε_W) and nonwave energy dissipation rates (ε_{NW}) in the AE rough experiments (unit: J). (a-b): AE control experiment; (c-d): AE rough experiment.

Fig. 17. Comparison between results from the non-hydrostatic and hydrostatic models.

TABLE 1. Model experiments (AE–experiment initialized with an anticyclonic eddy; CE–experiment initialized with a cyclonic eddy; Random–experiment initialized with a sea of random eddies; ctrl–control experiment with a smooth topography; rough–experiment with a rough topography).

Experiments	AE ctrl	AE rough 1	AE rough 2	CE ctrl	CE rough	Random ctrl	Random rough
Topography	Smooth	Rough 1	Rough 2	Smooth	Rough 1	Smooth	Rough 1
Duration	200 days	200 days	180 days	200 days	200 days	300 days	300 days

TABLE 2. Mean probabilities of occurrence (%) of LOB (GI–gravitational instability; INI–inertial instability; SI–symmetric instability; AAI–anticyclonic-ageostrophic instability; KHI–Kelvin-Helmholtz instability).

	CE ctrl	CE rough	AE ctrl	AE rough 1	AE rough 2
GI	0.0214	0.0094	0.0953	0.0397	0.0398
INI	6.77e-05	0.0152	2.68e-06	0.0152	0.0156
SI	0.0066	0.0083	0.0027	0.0173	0.0146
AAI	0.0399	**0.3128**	0.0095	**0.3190**	**0.2891**
KHI	1.14e-05	0.0054	2.07e-04	0.0294	0.0279

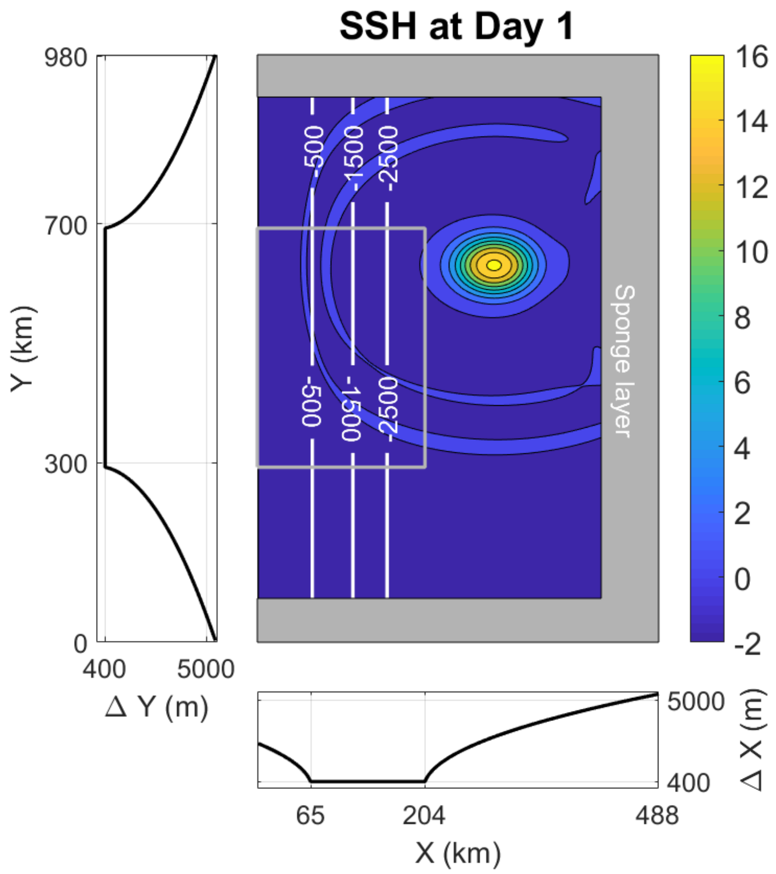

Fig. 1. The model domain for single eddy experiments with sponge layers at the southern, eastern and northern boundaries (gray shading). The spatially variable grid resolution in both horizontal directions is shown in the two side panels. The white contours represent the isobaths (m) of the smooth topography. The region near the western boundary inside the gray box is where the eddy energy budget analysis is conducted. The color shading in the main panel shows the SSH (cm) on day 1 in the experiment initialized with an anticyclonic eddy. The model domain for the experiment with a sea of random eddies is the same except that it is wider (717 km) in the zonal direction.

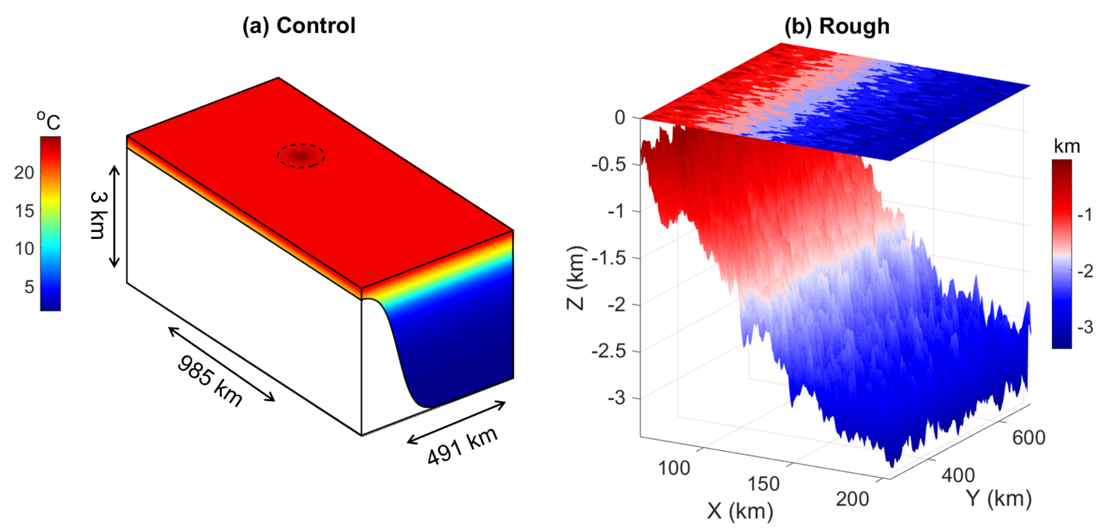

Fig. 2. Topography used in (a) control and (b) rough-topography experiments. The color shading in (a) shows the background temperature (°C) in the control experiment initialized with an anticyclonic eddy. The color shading in (b) shows the bathymetry (km) in the rough-topography experiment.

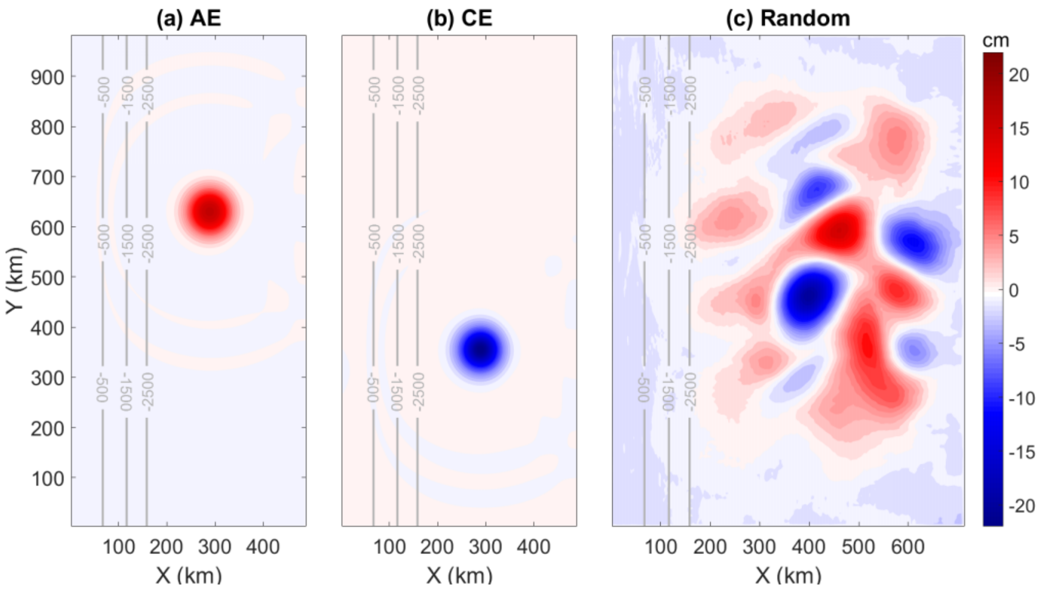

Fig. 3. SSH (cm) fields on day 1 in experiments initialized with (a) a single AE, (b) a single CE and (c) a sea of random eddies. Gray lines represent the isobaths (m) of the smooth topography.

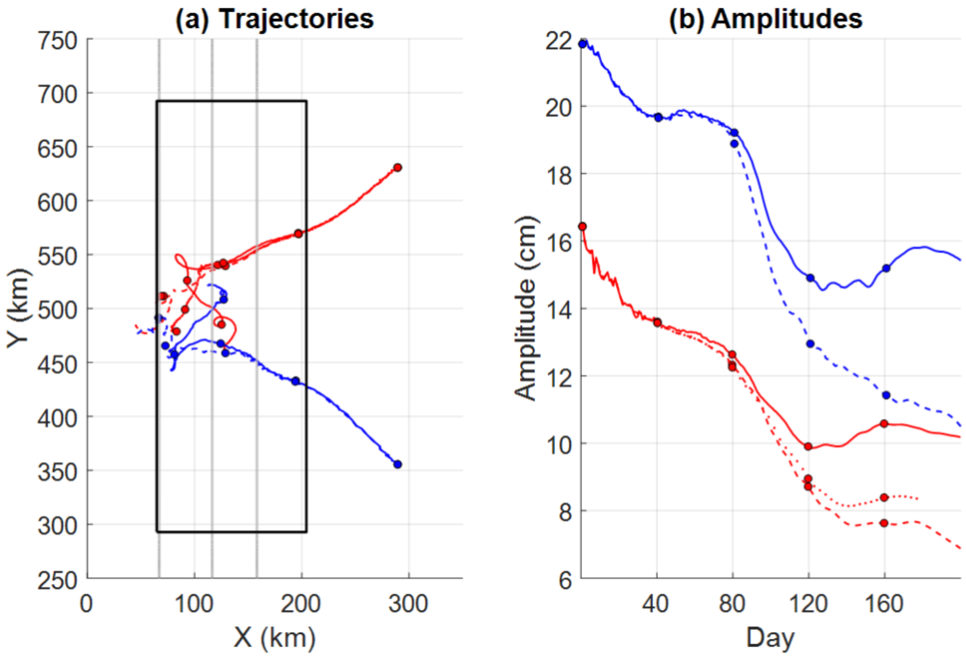

Fig. 4. Eddy (a) trajectories and (b) amplitudes in the control (solid), rough 1 (dashed) and rough 2 (dotted) experiments initialized with either a single AE (red) or CE (blue). Gray contours in (a) show the isobaths (m) of the smooth topography and the black box encloses the high-resolution (400 m) region where the synthetically-generated rough topography is added to the smooth hyperbolic tangent function in the rough-topography experiments. The blue and red dots with black circles in (a) and (b) indicate the eddy locations and amplitudes every 40 days.

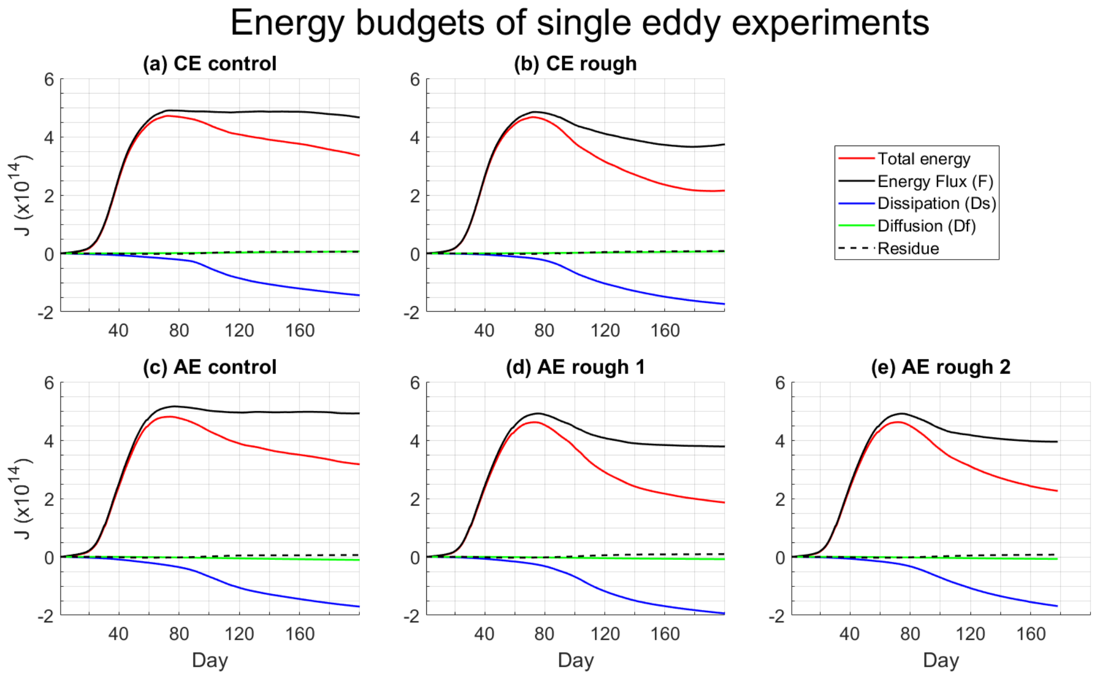

Fig. 5. Time series of cumulative energy flux into the gray box near the western boundary in Fig. 1 (black solid), cumulative energy dissipation within the box (blue), cumulative diffusive energy flux across the boundaries of the box (green), total energy within the box (red) and the residue (black dashed) for the five single eddy experiments.

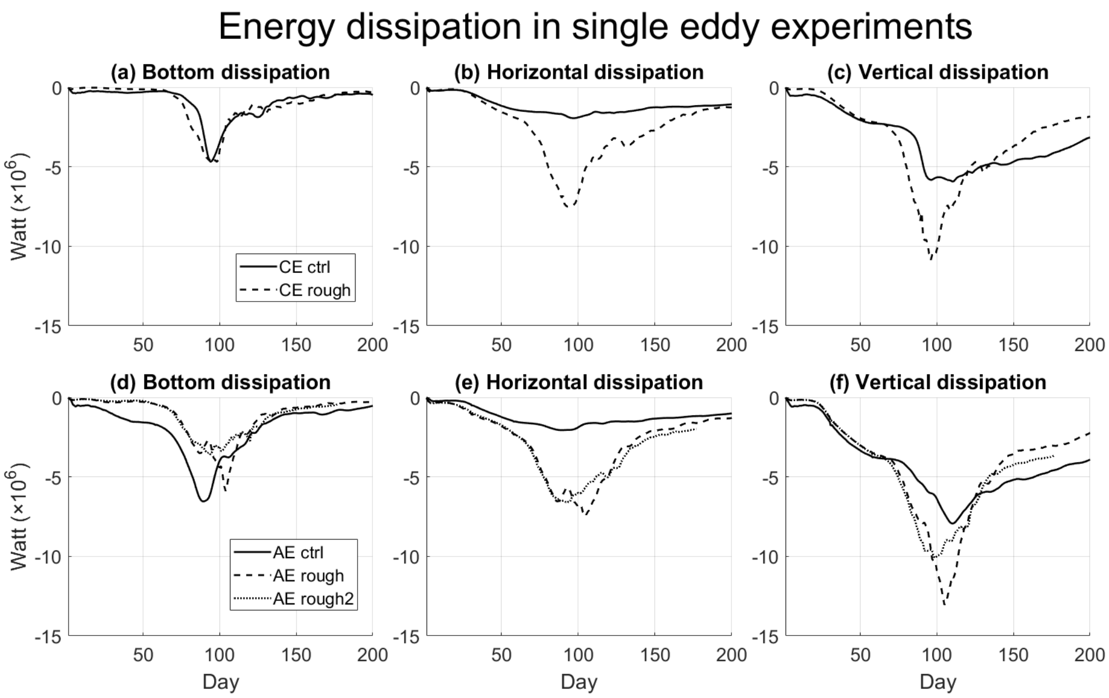

Fig. 6. Instantaneous bottom frictional dissipation and interior viscous dissipation in five single eddy experiments. The upper panels are for the CE experiments and lower panels for the AE experiments. Solid, dashed and dotted curves represent results from the control, rough 1 and rough 2 experiments, respectively.

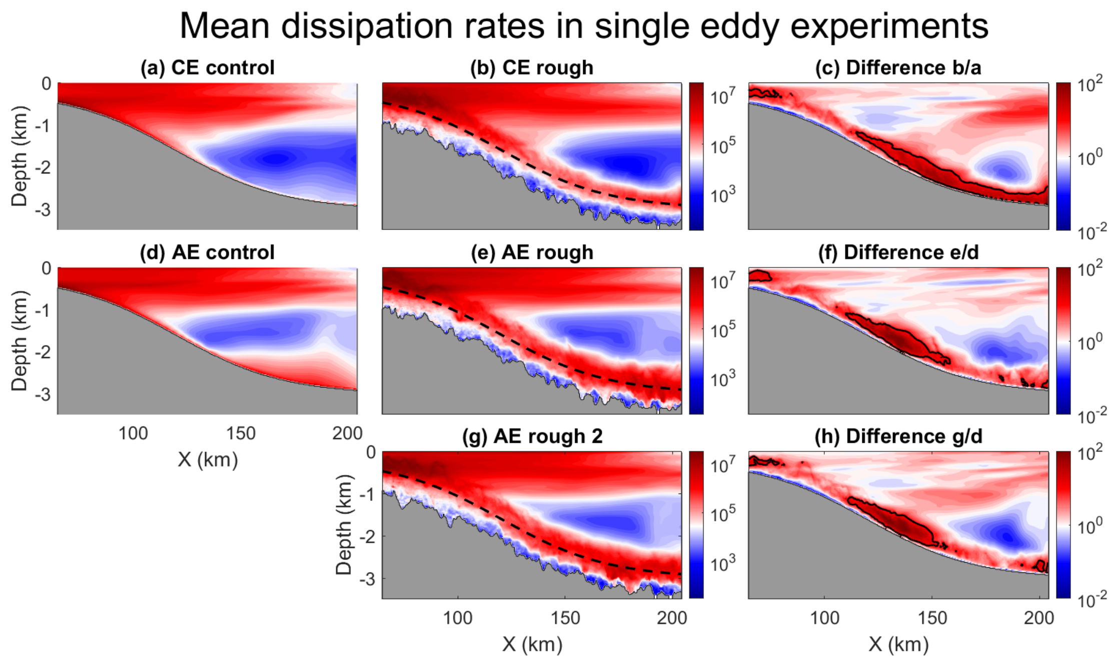

Fig. 7. Along slope mean dissipation rate (unit: J) integrated during day 81-120 in single eddy experiments. (a) and (b) are for the CE control and rough-topography experiments, respectively. (c) is ratio between (a) and (b), i.e., (b) divided by (a), and the black lines in (c) are contours of ten; (d-f) are the same as (a-c) but for the AE control and AE rough 1 experiments; (g-h) are the same as (b-c) but for the AE rough 2 experiment.

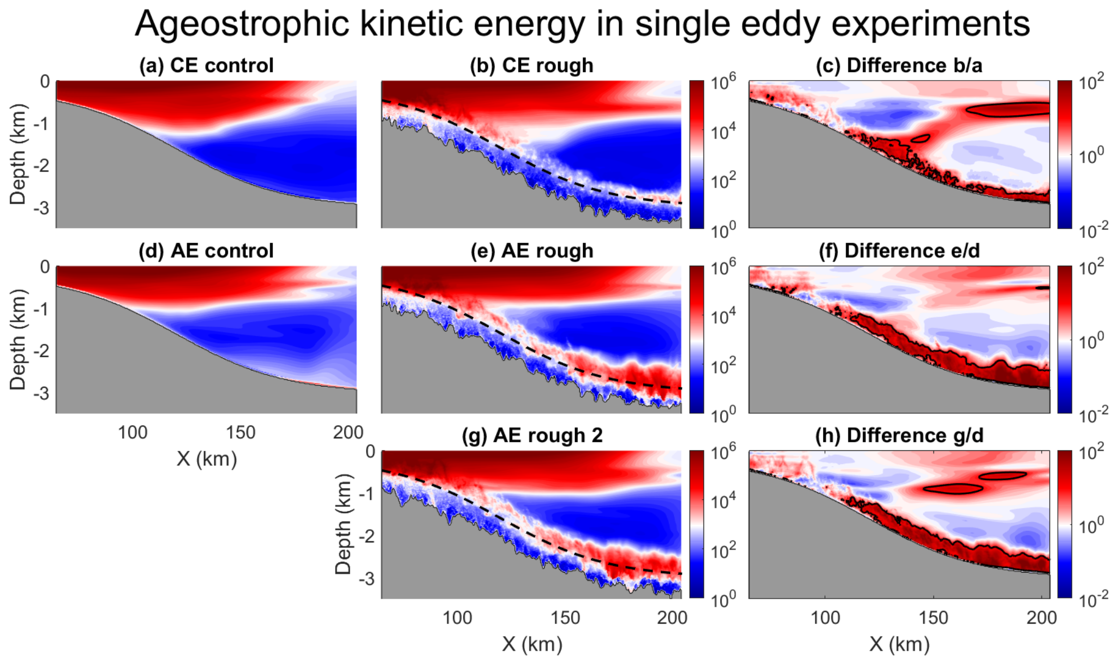

Fig. 8. Along slope mean ageostrophic kinetic energy (unit: J) integrated during day 81-120 in single eddy experiments. (a) and (b) are for the CE control and rough-topography experiments, respectively. (c) is the ratio between (a) and (b), i.e., (b) divided by (a), and the black lines in (c) are contours of ten; (d-f) are the same as (a-c) but for the AE control and AE rough 1 experiments; (g-h) are the same as (b-c) but for the AE rough 2 experiment.

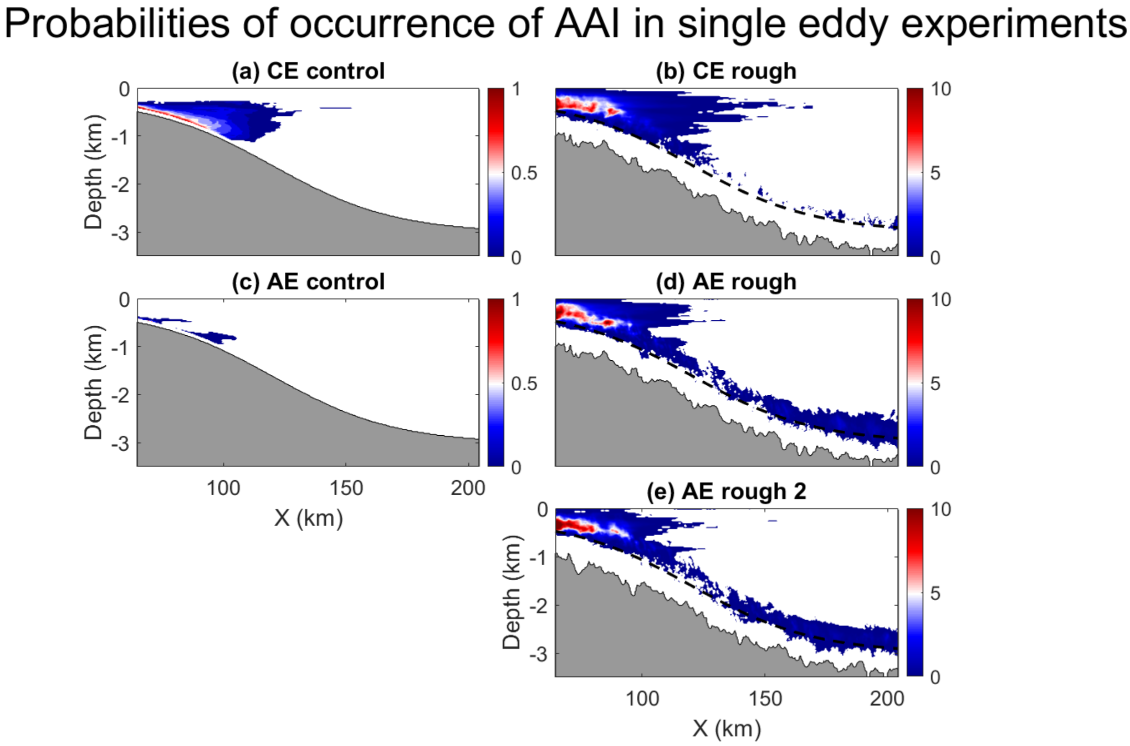

Fig. 9. Along slope mean probabilities of occurrence of AAI during day 81-120. (a) CE control; (b) CE rough; (c) AE control; (d) AE rough 1; (e) AE rough 2.

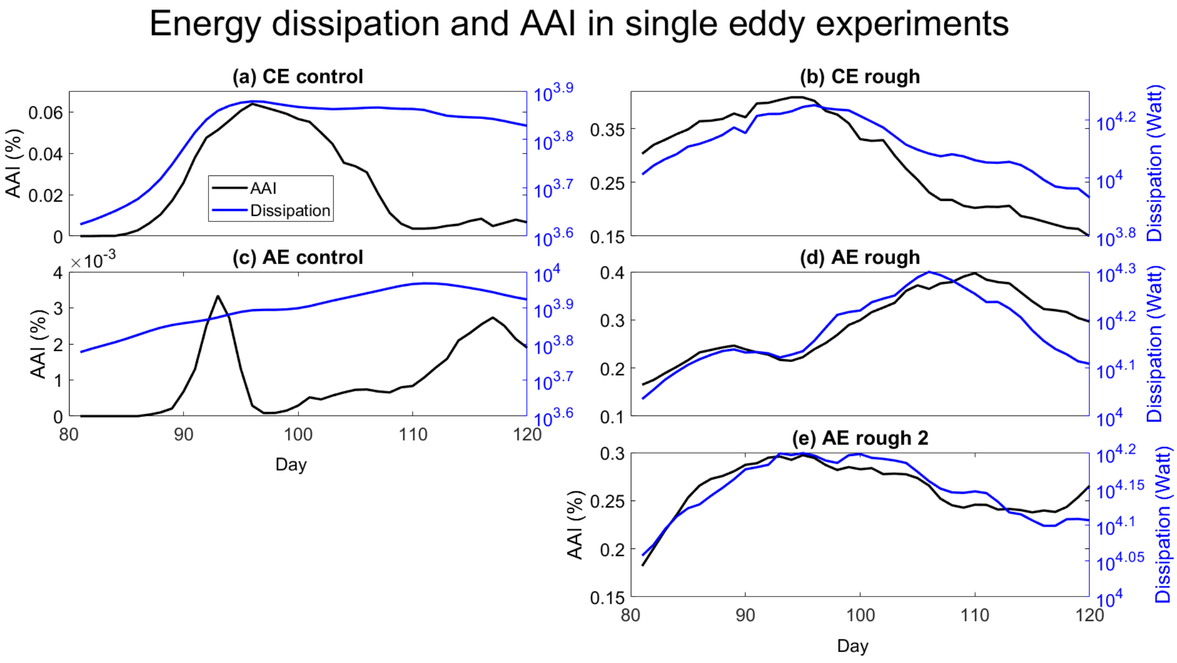

Fig. 10. Time series of occurrence of AAI (black) and viscous energy dissipation (blue; watt) during day 81-120 in the five single eddy experiments.

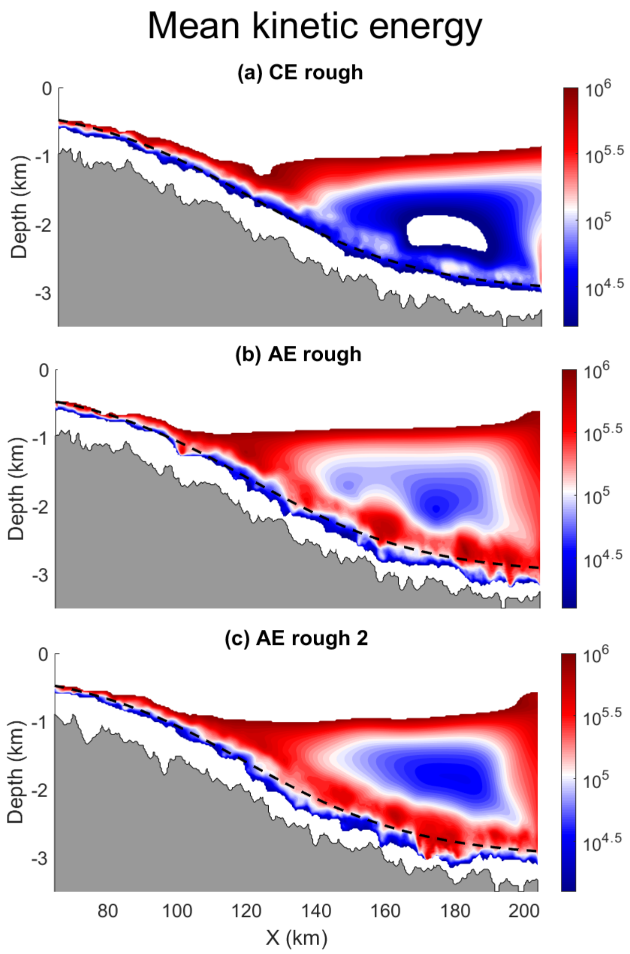

Fig. 11. Along slope mean kinetic energy (J) during day 81-120 in single eddy experiments. Only kinetic energy with values within the colorbar range limits is shown.

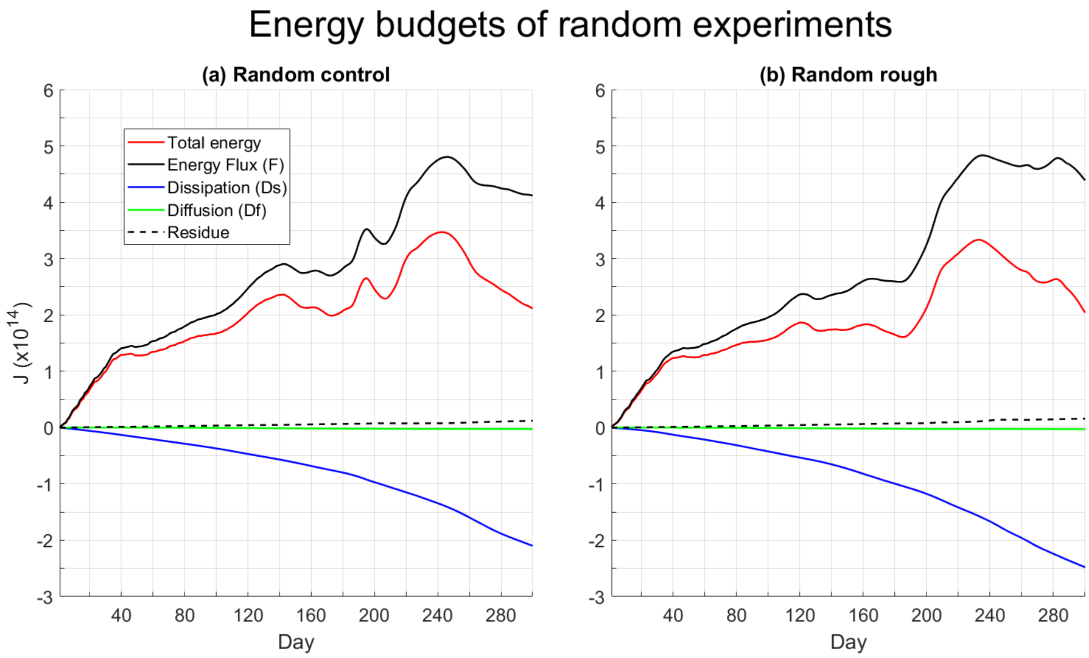

Fig. 12. Time series of cumulative energy flux into the gray box near the western boundary in Fig. 1 (black solid), cumulative energy dissipation within the box (blue), cumulative diffusive energy flux across the boundaries of the box (green), total energy within the box (red) and the residue (black dashed) for the experiments initialized with a sea of random eddies.

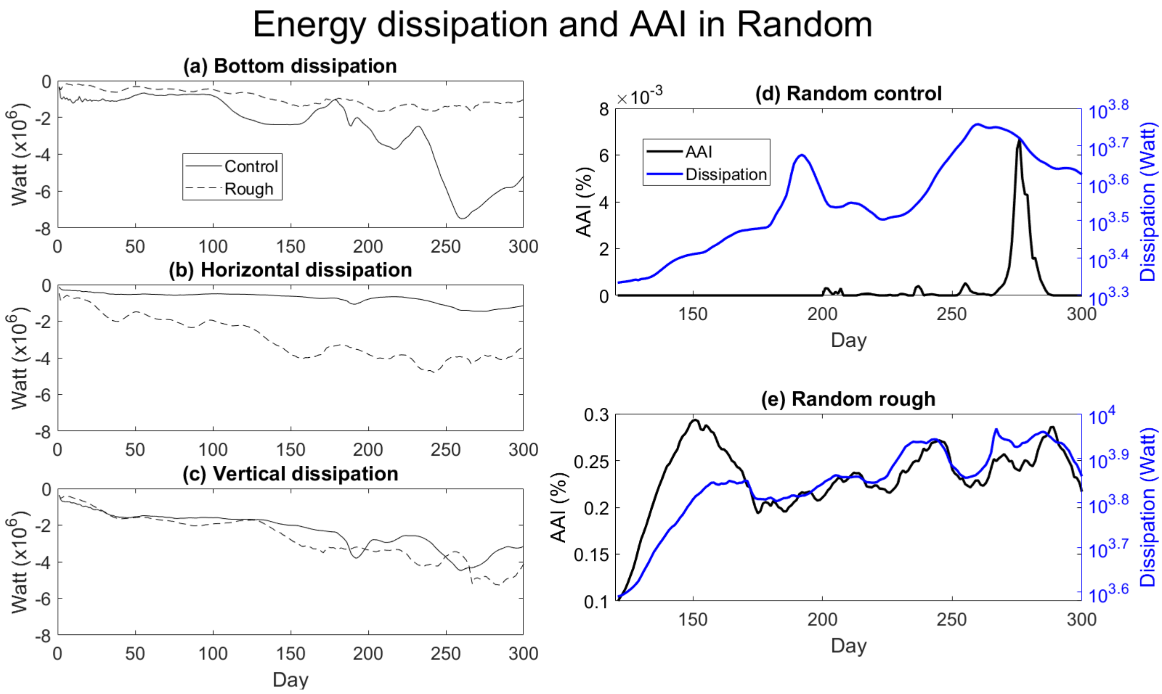

Fig. 13. Instantaneous (a) bottom frictional dissipation, (b) horizontal viscous dissipation, (c) vertical viscous dissipation and (d-e) relationship between energy dissipation and probabilities of occurrence of AAI in the two experiments initialized with a sea of random eddies; and the relationship between dissipation (unit: watt) and AAI (percent) for (d) control case; (e) rough case.

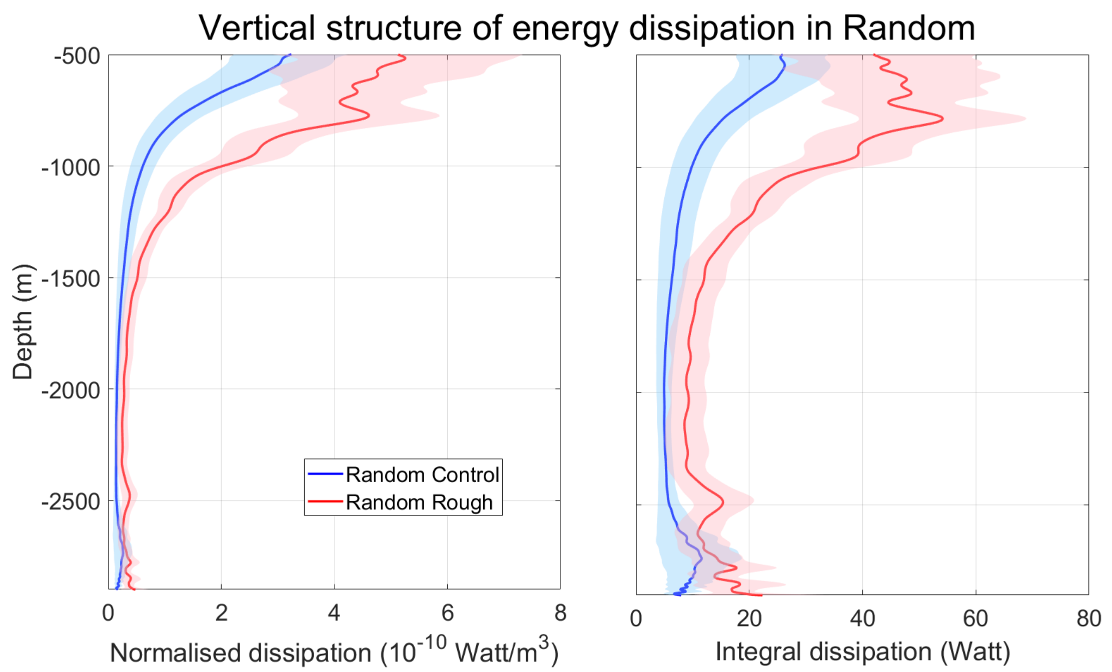

Fig. 14. (a) Volume-normalised and (b) volume-integrated energy dissipation rates as a function of depth during day 121-300 in the sea of random eddies experiments. Blue (red) line shows the result from the experiment with a smooth (rough) topography, and the color shading represents the standard deviation.

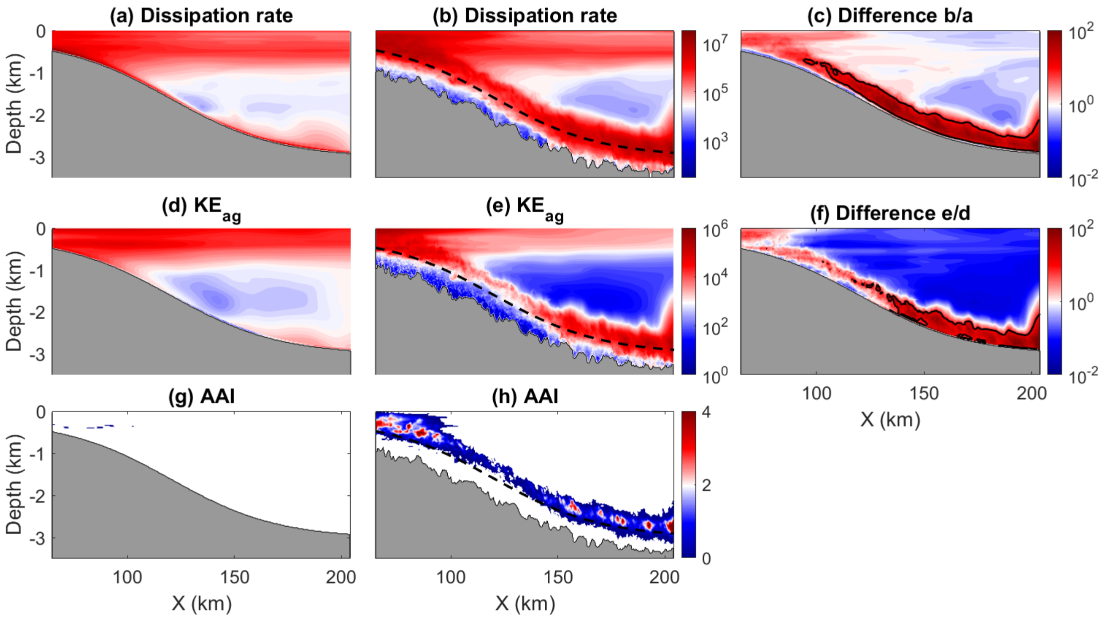

Fig. 15. Along slope mean dissipation rate (a-c; unit: J), ageostrophic kinetic energy (d-f; unit: J) and probabilities of occurrence of AAI (g-h) integrated over day 201-240 in the sea of random eddies experiments. Black lines in c & f represent contours of ten.

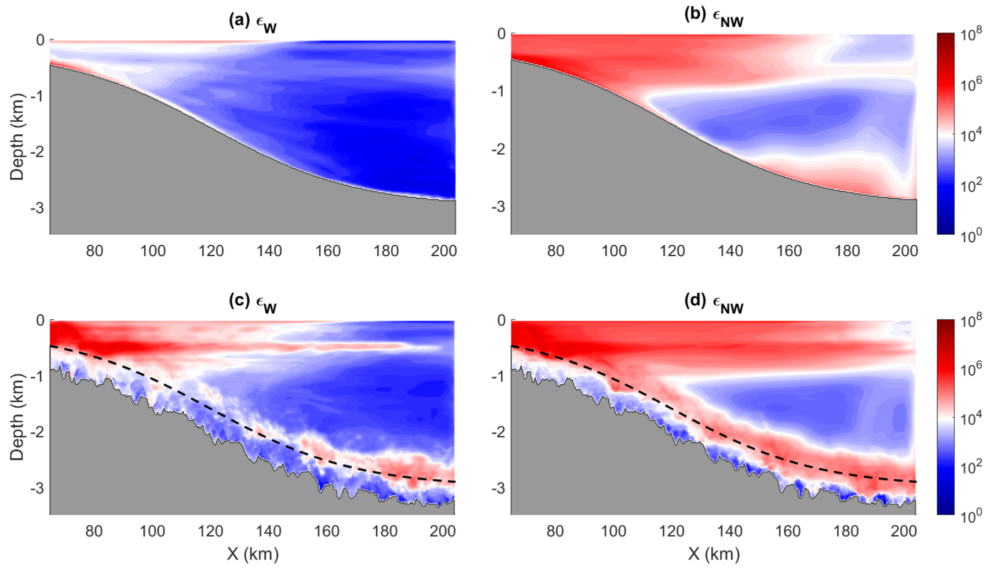

Fig. 16. Wave (ε_W) and nonwave (ε_{NW}) energy dissipation rates integrated during day 83-87 in AE control (a-b) and AE rough (c-d) experiments (unit: J).

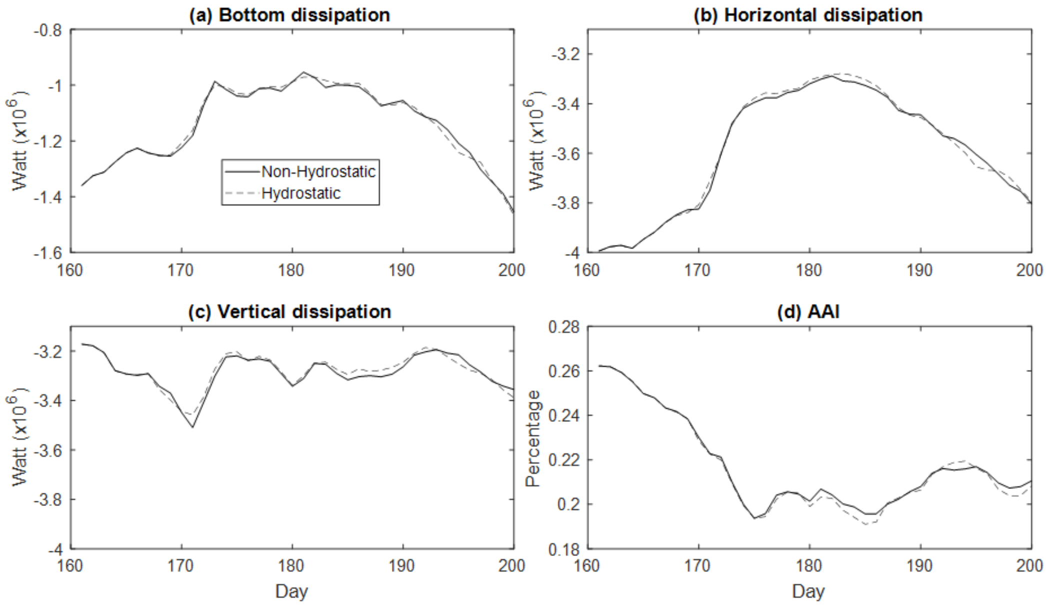

Fig. 17. Comparison between results from the non-hydrostatic and hydrostatic models.